Petroleum Science 22 (2025) 2203–2214

Contents lists available at ScienceDirect

Petroleum Science

journal homepage: www.keaipublishing.com/en/journals/petroleum-science

Original Paper

Hydrocarbon generation reaction kinetics study on supercritical water conversion of centimeter sized medium and low maturity organic-rich shale

Tian Xie [a], [**], Qiu-Yang Zhao [b], [*], Hui Jin [b], Ye-Chun Wang [b], Lie-Jin Guo [b]

[a] College of New Energy, Xi'an Shiyou University, Xi'an, 710065, Shaanxi, China
[b] State Key Laboratory of Multiphase Flow in Power Engineering, Xi'an Jiaotong University, Xi'an, 710049, Shaanxi, China

ARTICLE INFO

Article history:
Received 29 September 2024
Received in revised form
22 December 2024
Accepted 25 February 2025
Available online 27 February 2025

Edited by Min Li

Keywords:
Organic-rich shale
Supercritical water
Conversion
Hydrocarbon generation
Kinetics

ABSTRACT

Accurate prediction of the composition of pyrolysis products is the prerequisite for achieving directional regulation of organic-rich shale pyrolysis and conversion products. In this paper, the classical segmented pyrolysis kinetics model and a new refined pyrolysis kinetics model were used to forecast the composition distribution of hydrocarbon generation products co-heated by supercritical water and medium and low maturity organic-rich shale. The prediction accuracy of the two reaction kinetics models for the composition of pyrolysis products of organic-rich shale was compared. The reaction path of hydrocarbon generation in centimeter sized organic-rich shale under the action of supercritical water was identified. The results show that the prediction accuracy of the classical segmented pyrolysis kinetics model was poor at the initial stage of the reaction, and gradually increased with increasing time. The prediction error can reach less than 25% when the reaction time was 12 h. The new refined model of reaction kinetics established is better than the classical reaction kinetics model in predicting the product distribution of pyrolysis oil and gas, and its prediction error is less than 14% in this paper. The reaction paths of hydrocarbon generation in centimeter sized organic-rich shale under supercritical water conversion mainly include organic-rich shale directly generates asphaltene and saturated hydrocarbon, asphaltene pyrolysis generates saturated hydrocarbon, aromatic hydrocarbon and resin, saturated hydrocarbon, aromatic hydrocarbon and resin polymerization generates asphaltene, and saturated hydrocarbon, resin and asphaltene generates gas. The reason for the difference of centimeter sized and millimeter sized medium and low maturity organic-rich shales hydrocarbon generation in supercritical water is that the increase of shale size promotes the reaction path of polymerization of saturated hydrocarbon and aromatic hydrocarbon to asphaltene.

1. Introduction

Energy security is troubling mankind. Oil is important components of energy. As non-renewable resources, conventional oil is gradually depleted. However, the development of human economy and society cannot be separated from oil, there must be new substitutes. Therefore, people begin to pay attention to the unconventional oil resources of medium and low maturity shale oil (MLMSO) (Zou et al., 2013; Jin et al., 2019; Zhao et al., 2020). The characteristics of MLMSO is that most of it is stored in the form of solid kerogen in the shale porous medium, which together with the shale porous medium forms the medium and low maturity organic-rich shale (MLMOS) system (Guo et al., 2024). This part of the oil resource is difficult to flow, so there are a lot of ways that people are thinking about to make this resource flow. All these methods belong to the category of thermal conversion methods (Deng et al., 2012; Hou et al., 2020; Kang et al., 2020a, 2020b). However, despite achieving varying degrees of hydrocarbon generation efficiency, most of these technologies suffer from issues such as low conversion efficiency, high energy consumption, or difficulties in control (Akiya and Savage, 2002; Tang et al., 2013; Hu et al., 2024).

The excellent performance of supercritical water (SCW) in the field of macromolecular organic matter conversion has attracted

---

[*] Corresponding author.
[**] Corresponding author.
E-mail addresses: xietian@xsyu.edu.cn (T. Xie), qyzhao@mail.xjtu.edu.cn (Q.-Y. Zhao).

https://doi.org/10.1016/j.petsci.2025.02.020

the attention of petroleum workers, and it has been applied to the field of in-situ conversion of MLMOS (Reddy et al., 2014; Rodriguez and Kruse, 2018; Rana et al., 2019; Wang et al., 2021). Its most unique properties are undoubtedly its strong heat-carrying capacity and its hydrogen supply capacity as a reactant (Weingärtner and Franck, 2005; Zhao et al., 2018; Guo et al., 2015). At the same time, the problems related to SCW in-situ conversion MLMOS to generate hydrocarbon have been widely studied (Yanik et al., 1995; Hu et al., 1999; Veski et al., 2006; Nasyrova et al., 2020; Liang et al., 2021). It mainly focuses on the following aspects. The first is the research and development and design of the transformation experimental system. At present, two kinds of static and dynamic experimental systems have been initially formed, and the static system is characterized by simple operation flow. The dynamic system is characterized by on-line testing of the product. The second is the influencing factors and the composition of the conversion products. Physical properties of SCW, artificially controlled working conditions and reactant size are the key factors affecting the conversion process. Oil phase products are mainly asphaltene, gas phase products are mainly methane, hydrogen, carbon dioxide and so on. Some water-soluble organic substances are also formed.

In addition, in order to explore the reaction path of hydrocarbon generation by pyrolysis of MLMOS, the kinetic characteristics of hydrocarbon generation by pyrolysis of MLMOS have been widely investigated (Brandt, 2008; Wang et al., 2014; Sun et al., 2019; Kang et al., 2020, 2024; Xie et al., 2023a,b; Chen et al., 2024). The predecessors mainly focus on the model building, the calculation of the model and so on. The existing models are mainly parallel reaction models under a large number of assumptions, and a few people have established the total first-order, segmented first-order and total N-order pyrolysis reaction kinetics models. Among them, the parallel reaction model consisting of many first-order reactions can describe the process of hydrocarbon generation most succinctly and accurately. Li and Yue (2003) established a reaction kinetics model consisting of several parallel first-order reactions, and found that there was an exponential relationship between product conversion rate and activation energy through fitting and solving. In addition, many parallel reaction models were established and fitted solutions to obtain kinetic parameters, thus revealing the mechanism of pyrolysis hydrocarbon generation (Bar et al., 1988; Huang et al., 2023; Zheng et al., 2023). In addition to the model method, there are some model-free linear fitting methods to obtain the kinetic parameters (Ozawa, 1965; Flynn and Wall, 1966; Sun et al., 2015). Such as Ozawa-flynn-wall (OFW) integral method, kissinger-akhira-sunose (KAS) method and isothermal induction stage method. Model-free method is a method that can obtain the kinetic parameters without assuming the mechanism function, avoiding the determination of the specific form of the mechanism function $f(\alpha)$.

There is another important discovery about water in previous studies, that is, whether water is involved in the process of hydrocarbon generation in MLMOS pyrolysis will have a significant impact on the kinetic parameters (Fang et al., 2012; Lin et al., 2016; Ma and Li, 2018; Zhao et al., 2022). Water can change the reactivity of each single reaction in the pyrolysis of MLMOS, and cause the fluctuation of energy required in the reaction process (Zhao et al., 2022).

Overall, the pyrolysis of MLMOS is a very complicated process. The pyrolysis process can be divided into many reactions, and the energy required for the successful occurrence of different reactions is different. The traditional kinetics model of MLMOS pyrolysis for hydrocarbon generation was established on the basis of the segmented pyrolysis hypothesis, which is characterized by a highly lumped and macroscopic view of the substances in the reaction system. However, the existing models do not consider the presence of SCW, and the addition of SCW will undoubtedly complicate the pyrolysis process. In addition, most of the reaction kinetics models established by predecessors are based on millimeter scale shale pyrolysis experimental data. However, this is quite different from the actual field size, mainly due to the difficulty of fracturing the fracture network unit to the millimeter scale in the shale field. Therefore, in order to more truly describe the pyrolysis process of MLMOS under field conditions, this paper mainly used the experimental data of hydrocarbon generation of centimeter sized MLMOS under SCW in-situ conversion, and firstly established a classical four-phase lumped reaction kinetic model of solid-oil-gas-water. In addition, a new refined reaction kinetics model was proposed in this paper, in order to find out the reaction path of hydrocarbon generation under SCW in-situ conversion of centimeter sized MLMOS, and improve the prediction accuracy of hydrocarbon product distribution after conversion of organic-rich shale.

2. Experiment section

2.1. Material

The MLMOS used in this paper is taken from ShanBei, China. Table 1 shows its detail characteristics. The initial shale characteristics before the reaction were measured using an elemental analyzer (Elementar Vario Macro cube on CHNS mode) and a proximate analyzer (Kaiyuan Instrument 5E-MAG6700 on TGA mode). The type of kerogen in MLMOS was judged by the element composition. The size range of MLMOS used in this experiment is 10–40 mm.

2.2. Method

The experimental system used in this paper has been described in detail in the team's previous research (Xie et al., 2023a, 2023b). The experimental system diagram is shown in Fig. 1. The reaction system can be divided into leak detection device, monitoring device and heating device.

The experimental steps of this paper have also been introduced in detail in the previous work (Xie et al., 2023a, 2023b), and this paper will briefly describe them. The procedure for the experiment is outlined below: Initially, a measured amount of MLMOS and purified water were added into the reactor. Subsequently, inert gas was employed to check for any leaks. Once a leak-proof seal was confirmed, the heating mechanism was activated. The process timer was initiated upon reaching the target reaction temperature, and the heating was ceased once the predetermined duration was completed. The reactor is then immediately cooled to room temperature by a water bath. It should be noted that the cooling time of the water bath is not included in the reaction time of the experimental design, and the cooling time of the water bath is very short and almost negligible. Once the interior temperature of the reactor matched room temperature, it was opened, and the gaseous products were gathered using an airbag. The liquid components and solid residues within the reactor were subsequently transferred to a centrifuge tube, to which carbon disulfide (CS_2) was added before proceeding with centrifugation. Post-centrifugation, the tube separated into three distinct layers: water at the top, a CS_2 oil solution in the middle, and shale residue at the bottom. The CS_2 oil solution was then placed in a drying oven set at 46 °C to evaporate the CS_2, leaving behind the oil. The solid residue was treated in a drying oven at 100 °C to remove any water and CS_2. Throughout the experiment, the computer, data acquisition system, and temperature and pressure sensors continuously monitored and documented the internal conditions of the reactor. The total carbon

Table 1
Proximate analysis and elemental analysis of the shale.

Proximate analysis, wt%				Elemental analysis, wt%				R_o	Kerogen type
moisture	ash	volatile matter	fixed carbon	carbon[a]	hydrogen	nitrogen	sulphur	0.52	II
1.56	72.698	10.53	15.228	16.423	1.55	1.07	5.13		

[a] The organic carbon content of the experimental samples used in this paper is 16.25 wt%.

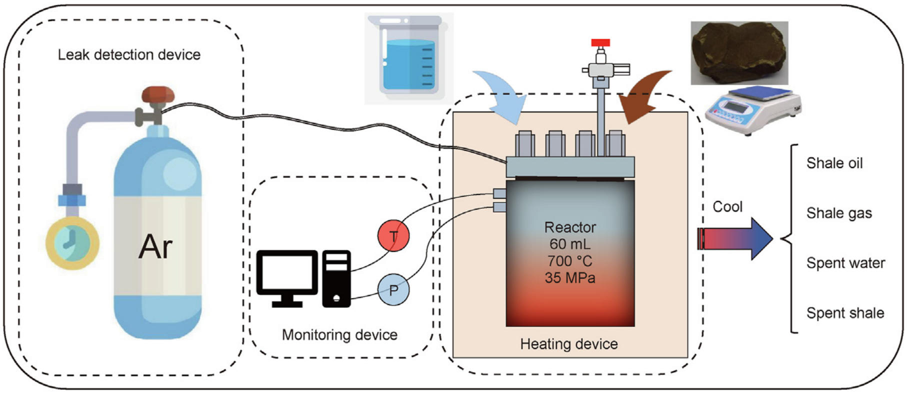

Fig. 1. Experimental system diagram.

content of solids was analyzed by grinding the solid sample to less than 100 mesh and weighing 50 mg into the element analyzer (Elementar vario MACRO cube). The resulting oil was analyzed for its composition using a SARA analyzer (IATROSCAN MK-6S) and an elemental analyzer (Elementar vario Macro cube). SARA analysis is to burn soluble organic samples that are non-volatile at room temperature in a flame, dilute them with solvent and point them onto a thin layer rod coated with silica gel and alumina adsorption, remove the solvent and put them into the corresponding development tank for development and separation under a certain saturated vapor pressure environment. After sample development, the thin layer rods are sequentially entered into the hydrogen flame detector, and a certain scanning speed is selected for combustion ionization to obtain the corresponding component ion flow diagram (chromatogram). The gaseous products were characterized by gas chromatography (Agilent 7890a), which is equipped with a thermal conductivity detector and a flame ionization detector. The capillary column C2000 purchased from Lanzhou Institution of Chemical Physics in China and the column Agilent J&W HP-PLOT Al_2O_3 KCl was used for analyzing the fractions of H_2, CO, CH_4, CO_2, and gaseous light hydrocarbons (C_{2+}). High-purity argon was used as a carrier gas with a flow rate of 30 $mL\cdot min^{-1}$.

2.3. Construction of reaction kinetic model

2.3.1. Reaction rate description

As we all know, the purpose of the study of reaction kinetics is to reveal the reaction mechanism. The most important step is to obtain the kinetic parameters. However, the complexity of material composition of MLMOS makes its reaction during pyrolysis more complicated, so some necessary assumptions must exist. Assuming that the reaction process is an isothermal homogeneous reaction, the reaction rate can be expressed by the following equation (Xie et al., 2023a, 2023b). The kinetic parameters can be obtained by fitting and solving the following Eq. (1).

$$\frac{dx}{dt} = k(T)\cdot f(x) = A\exp(-E_a/RT)\cdot f(x) \tag{1}$$

Where: t—reaction time; x—Concentration; $k(T) = A\exp(-E_a/RT)$—reaction rate constant; E_a—activation energy; A—prefactor; R—molar gas constant; T—temperature; $f(x)$—mechanism function (Xie et al., 2023a, 2023b).

2.3.2. Model building

This paper includes two kinetic models of hydrocarbon generation, both of which are based on lumping idea. One is a kinetics model based on classical segmented pyrolysis theory, and the other is a new refined reaction kinetics model proposed by our team.

Classical segmented reaction kinetics model for hydrocarbon generation by pyrolysis of organic-rich shale.

It is assumed that there are only 4 kinds of substances in the reaction system, which are MLMOS and its intermediate products (denoted as SO), oil phase products (denoted as O), gas phase products (denoted as G) and water phase substances (denoted as W). In addition, it is assumed that the process of converting MLMOS and other intermediates produced by pyrolysis into oil phase products is reversible.

Based on the classical pyrolysis kinetics theory and the above assumptions, the co-heating process of hydrocarbon generation between MLMOS and SCW consists of three parallel first-order reactions was proposed. Fig. 2 shows the reaction network in this kinetic model.

According to the classical segmented reaction kinetics model for hydrocarbon generation by pyrolysis of organic-rich shale. The main reactions between MLMOS and SCW are shown in Eqs. (2)–(4).

$$SO + W \underset{k_{1r}}{\overset{k_{1f}}{\rightleftarrows}} O \tag{2}$$

$$SO + W \xrightarrow{k_2} G \tag{3}$$

$$O + W \xrightarrow{k_3} G \tag{4}$$

Because it is difficult to obtain the correct value of the mass of water

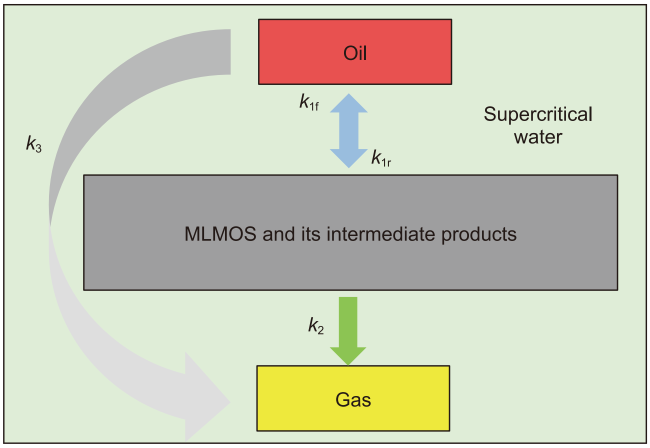

Fig. 2. Reaction network based on the theory of segmented pyrolysis of MLMOS.

in the reactor after the reaction, some simplified treatment is done here. Suppose that the concentration of water in the reaction system is a constant value 1. According to the reaction path shown by the reaction network, the change of the composition distribution of the four substances in the reaction system with the reaction time is expressed by Eqs. (5)–(8) respectively. It should be noted that k_{1f} represents the reaction rate constant of the forward reaction and k_{1r} represents the reaction rate constant of the reverse reaction.

$$\frac{dC_O}{dt} = k_{1f}C_{SO} - k_{1r}C_O - k_3C_O \tag{5}$$

$$\frac{dC_{SO}}{dt} = -k_{1f}C_{SO} + k_{1r}C_O - k_2C_{SO} \tag{6}$$

$$\frac{dC_G}{dt} = k_2C_{SO} + k_3C_O \tag{7}$$

$$\frac{dC_W}{dt} = -k_{1f}C_{SO} - k_2C_{SO} - k_3C_O + k_{1r}C_O \tag{8}$$

New refined reaction kinetics model for hydrocarbon generation by pyrolysis of MLMOS.

In order to more accurately explain the complex reaction path involved in the co-pyrolysis reaction of MLMOS with SCW, and to achieve accurate prediction and effective control of hydrocarbon generation products, the model was constructed based on the following assumptions.

1) According to the lumped parameter idea, the oil phase products were divided into four parts, respectively saturated hydrocarbons, aromatics, resins and asphaltenes. in this study, the MLMOS and other intermediates generated during pyrolysis process are regarded as a comprehensive phase (SO). All gas products are also treated as another composite phase (G). Therefore, in this reaction model, the reactants and products involved can be generalized as saturated hydrocarbons (Sa), aromatics (Ar), resins (Re), asphaltenes (As), water (W), MLMOS and other intermediates (SO), and natural gas (G).

2) It is assumed that the As in many reactions are hydrolyzed to produce Sa, Ar and Re are reversible, and that all reactions are first-order reactions.

According to the above hypothesis, the co-heating process of hydrocarbon generation between MLMOS and SCW is composed of eleven parallel first-order reactions. The reaction network is shown in Fig. 3.

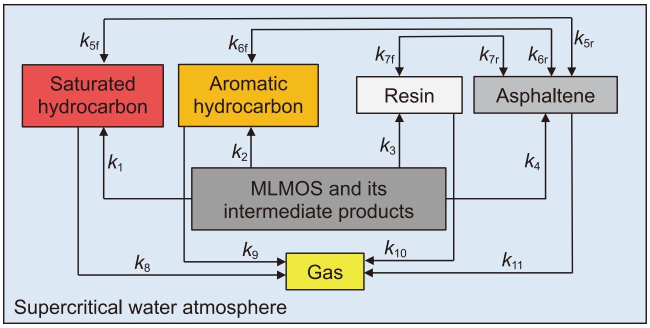

Fig. 3. Reaction network of organic-rich shale in SCW atmosphere.

The main reaction between MLMOS and SCW is shown in the following equations:

$$\mathrm{SO} + \mathrm{W} \xrightarrow{k_1} \mathrm{Sa} \tag{11}$$

$$\mathrm{SO} + \mathrm{W} \xrightarrow{k_2} \mathrm{Ar} \tag{12}$$

$$\mathrm{SO} + \mathrm{W} \xrightarrow{k_3} \mathrm{Re} \tag{13}$$

$$\mathrm{SO} + \mathrm{W} \xrightarrow{k_4} \mathrm{As} \tag{14}$$

$$\mathrm{As} + \mathrm{W} \underset{k_{5r}}{\overset{k_{5f}}{\rightleftarrows}} \mathrm{Sa} \tag{15}$$

$$\mathrm{As} + \mathrm{W} \underset{k_{6r}}{\overset{k_{6f}}{\rightleftarrows}} \mathrm{Ar} \tag{16}$$

$$\mathrm{As} + \mathrm{W} \underset{k_{7r}}{\overset{k_{7f}}{\rightleftarrows}} \mathrm{Re} \tag{17}$$

$$\mathrm{Sa} + \mathrm{W} \xrightarrow{k_8} \mathrm{G} \tag{18}$$

$$\mathrm{Ar} + \mathrm{W} \xrightarrow{k_9} \mathrm{G} \tag{19}$$

$$\mathrm{Re} + \mathrm{W} \xrightarrow{k_{10}} \mathrm{G} \tag{20}$$

$$\mathrm{As} + \mathrm{W} \xrightarrow{k_{11}} \mathrm{G} \tag{21}$$

According to the above equations, the substances in the hydrocarbon generation reaction system are divided into seven main categories. In addition to SCW, gaseous substances and organic-rich shale and its pyrolysis intermediates, the model pays special attention to the four main oil production components: saturated hydrocarbons, aromatics, resins and asphaltenes. The model assumes that the concentration of water remains constant, always 1. As with typical reaction kinetics models, the mass ratios of these seven substances change over time, as described by Eqs. (22)–(28).

$$\frac{dC_{Sa}}{dt} = k_1C_{SO} + k_{5f}C_{As} - k_{5r}C_{Sa} - k_8C_{Sa} \tag{22}$$

$$\frac{dC_{Ar}}{dt} = k_2C_{SO} + k_{6f}C_{As} - k_{6r}C_{Ar} - k_9C_{Ar} \tag{23}$$

$$\frac{dC_{Re}}{dt} = k_3C_{SO} + k_{7f}C_{As} - k_{7r}C_{Re} - k_{10}C_{Re} \tag{24}$$

$$\begin{aligned}\frac{dC_{As}}{dt} = {} & k_4C_{SO} - k_{5f}C_{As} + k_{5r}C_{Sa} - k_{6f}C_{As} + k_{6r}C_{Ar} \\ & - k_{7f}C_{As} + k_{7r}C_{Re} - k_{11}C_{As}\end{aligned} \tag{25}$$

$$\frac{dC_{SO}}{dt} = -k_1C_{SO} - k_2C_{SO} - k_3C_{SO} - k_4C_{SO} \tag{26}$$

$$\frac{dC_{G}}{dt} = k_8C_{Sa} + k_9C_{Ar} + k_{10}C_{Re} + k_{11}C_{As} \tag{27}$$

$$\begin{aligned}\frac{dC_{W}}{dt} = {} & -k_1C_{SO} - k_2C_{SO} - k_3C_{SO} - k_4C_{SO} - k_{5f}C_{As} + k_{5r}C_{Sa} \\ & - k_{6f}C_{As} + k_{6r}C_{Ar} - k_{7f}C_{As} + k_{7r}C_{Re} - k_8C_{Sa} - k_9C_{Ar}k_{10}C_{Re} \\ & - k_{11}C_{As}\end{aligned} \tag{28}$$

3. Result and discussion

3.1. Components distribution of product

Figs. 4–6 shows the variation of product composition with increasing time (60–720 min) at temperatures of 380, 400 and 430 °C. It is noted that the pressure (P) and water-shale mass ratio (R) was kept constant in this paper ($P = 24$ MPa, $R = 1$). The results show that under the three temperature settings, the variation trend of the mass fraction (MF) of each component with time is generally the same. The MF of kerogen, resin and asphaltene showed a decreasing trend, while the MF of saturated hydrocarbon, aromatic hydrocarbon and gas showed an increasing trend with increasing time. It can also be seen from Figs. 4–6 that the influence of temperature on hydrocarbon generation characteristics. Take a time point as an example, such as 60 min. The MF of kerogen and the total MF of saturated hydrocarbons and aromatics decreased, while the total MF of resin, asphaltene and gas increased with increasing temperature. It can also be seen from Figs. 4–6 that when the reaction time is 60 min, the total MF of kerogen, saturated hydrocarbon and aromatic hydrocarbon gradually decreased, while the total MF of resin and asphaltene gradually increased with increasing temperature. Of course, the change trend of MF with temperature at this fixed time point can also basically represent the trend at other reaction time points. From the point of view of fuel products, the MF of oil recovery gradually increased with increasing time at 380 °C. The MF of oil recovery first increased and then decreased at 400 and 430 °C. This reflects the fact that higher temperatures lead to earlier peaks in oil production, and that more oil is converted to gas with increasing time.

3.2. Fitting and solving of kinetic parameters of hydrocarbon reaction

3.2.1. Calculation method of fitting solution

The classical pyrolysis kinetics involved in this paper was similar to the new refined pyrolysis kinetics parameters fitting method. The contents of each component of each time step were calculated

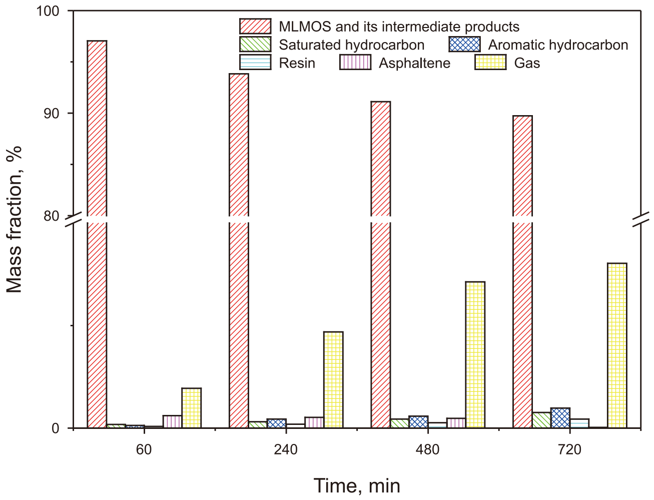

Fig. 4. The relationship between product composition distribution and time in the reaction system at 380 °C.

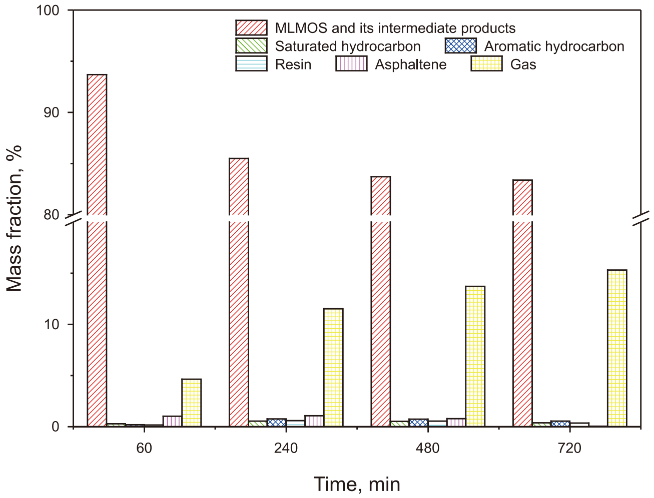

Fig. 5. The relationship between product composition distribution and time in the reaction system at 400 °C.

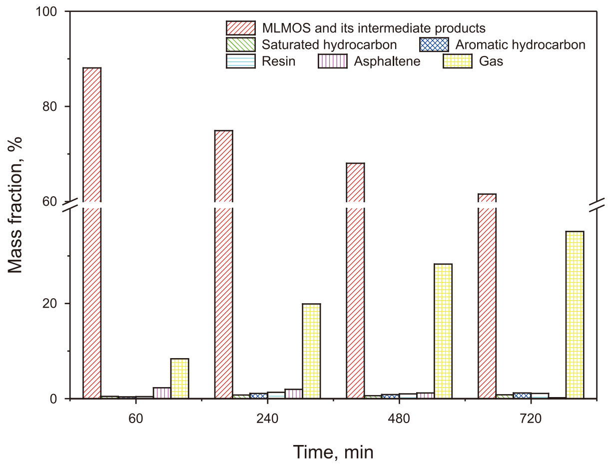

Fig. 6. The relationship between product composition distribution and time in the reaction system at 430 °C.

by Runge-Kutta fourth order method (Xie et al., 2023a,2023b). Due to the amounts of lumped products involved in the two reaction kinetics models was the difference, their calculation methods were also slightly different, as follows.

(1) For the classical segmented pyrolysis reaction kinetic model, the specific calculation method is shown in Eqs. (29)–(32).

$$\frac{\mathrm{d}C_{\mathrm{O}}}{\mathrm{d}t} = F_1(C_{\mathrm{O}}, C_{\mathrm{SO}}, C_{\mathrm{G}}, C_{\mathrm{W}}) \tag{29}$$

$$\frac{\mathrm{d}C_{\mathrm{SO}}}{\mathrm{d}t} = F_2(C_{\mathrm{O}}, C_{\mathrm{SO}}, C_{\mathrm{G}}, C_{\mathrm{W}}) \tag{30}$$

$$\frac{\mathrm{d}C_{\mathrm{G}}}{\mathrm{d}t} = F_3(C_{\mathrm{O}}, C_{\mathrm{SO}}, C_{\mathrm{G}}, C_{\mathrm{W}}) \tag{31}$$

$$\frac{\mathrm{d}C_{\mathrm{W}}}{\mathrm{d}t} = F_4(C_{\mathrm{O}}, C_{\mathrm{SO}}, C_{\mathrm{G}}, C_{\mathrm{W}}) \tag{32}$$

Use the step size h for the variable t, and construct the value in accordance with the rules of the function and the initial value:

$$\left[\begin{array}{l} A_{\mathrm{i}} = F_{\mathrm{i}}(C_{\mathrm{O}}, C_{\mathrm{SO}}, C_{\mathrm{G}}, C_{\mathrm{W}}) \\ B_{\mathrm{i}} = F_{\mathrm{i}}\left(C_{\mathrm{O}} + \frac{h}{2}A_1, C_{\mathrm{SO}} + \frac{h}{2}A_2, C_{\mathrm{G}} + \frac{h}{2}A_3, C_{\mathrm{W}} + \frac{h}{2}A_4\right) \\ C_{\mathrm{i}} = F_{\mathrm{i}}\left(C_{\mathrm{O}} + \frac{h}{2}B_1, C_{\mathrm{SO}} + \frac{h}{2}B_2, C_{\mathrm{G}} + \frac{h}{2}B_3, C_{\mathrm{W}} + \frac{h}{2}B_4\right) \\ D_{\mathrm{i}} = F_{\mathrm{i}}(C_{\mathrm{O}} + hC_1, C_{\mathrm{SO}} + hC_2, C_{\mathrm{G}} + hC_3, C_{\mathrm{W}} + hC_4) \end{array}\right. \tag{33}$$

Then the following iterative equation can then be used to calculate the MF of the oil phase material in section j+1.

$$C_{\mathrm{O}}^{j+1} = C_{\mathrm{O}}^{j} + \frac{h}{6}(A_1 + 2B_1 + 2C_1 + D_1) \tag{34}$$

where $j = 1,2 \cdots n$.

The iterative equations for the MF of organic-rich shale and its intermediate products, gas and water in the transformation process can also be derived by applying the above method. By repeating this process, the initial estimated value is used to gradually calculate the parameter value of each section until the entire calculation process is completed.

For the new refined reaction kinetics model, the specific calculation method is shown in Eqs. (35)–(41).

$$\frac{\mathrm{d}C_{\mathrm{Sa}}}{\mathrm{d}t} = F_1(C_{\mathrm{Sa}}, C_{\mathrm{Ar}}, C_{\mathrm{Re}}, C_{\mathrm{As}}, C_{\mathrm{SO}}, C_{\mathrm{G}}, C_{\mathrm{W}}) \tag{35}$$

$$\frac{\mathrm{d}C_{\mathrm{Ar}}}{\mathrm{d}t} = F_2(C_{\mathrm{Sa}}, C_{\mathrm{Ar}}, C_{\mathrm{Re}}, C_{\mathrm{As}}, C_{\mathrm{SO}}, C_{\mathrm{G}}, C_{\mathrm{W}}) \tag{36}$$

$$\frac{\mathrm{d}C_{\mathrm{Re}}}{\mathrm{d}t} = F_3(C_{\mathrm{Sa}}, C_{\mathrm{Ar}}, C_{\mathrm{Re}}, C_{\mathrm{As}}, C_{\mathrm{SO}}, C_{\mathrm{G}}, C_{\mathrm{W}}) \tag{37}$$

$$\frac{\mathrm{d}C_{\mathrm{As}}}{\mathrm{d}t} = F_4(C_{\mathrm{Sa}}, C_{\mathrm{Ar}}, C_{\mathrm{Re}}, C_{\mathrm{As}}, C_{\mathrm{SO}}, C_{\mathrm{G}}, C_{\mathrm{W}}) \tag{38}$$

$$\frac{\mathrm{d}C_{\mathrm{SO}}}{\mathrm{d}t} = F_5(C_{\mathrm{Sa}}, C_{\mathrm{Ar}}, C_{\mathrm{Re}}, C_{\mathrm{As}}, C_{\mathrm{SO}}, C_{\mathrm{G}}, C_{\mathrm{W}}) \tag{39}$$

$$\frac{\mathrm{d}C_{\mathrm{G}}}{\mathrm{d}t} = F_6(C_{\mathrm{Sa}}, C_{\mathrm{Ar}}, C_{\mathrm{Re}}, C_{\mathrm{As}}, C_{\mathrm{SO}}, C_{\mathrm{G}}, C_{\mathrm{W}}) \tag{40}$$

$$\frac{\mathrm{d}C_{\mathrm{W}}}{\mathrm{d}t} = F_7(C_{\mathrm{Sa}}, C_{\mathrm{Ar}}, C_{\mathrm{Re}}, C_{\mathrm{As}}, C_{\mathrm{SO}}, C_{\mathrm{G}}, C_{\mathrm{W}}) \tag{41}$$

Use the step size h for the variable t, and construct the value in accordance with the rules of the function and the initial value:

$$\left[\begin{array}{l} A_{\mathrm{i}} = F_{\mathrm{i}}(C_{\mathrm{Sa}}, C_{\mathrm{Ar}}, C_{\mathrm{Re}}, C_{\mathrm{As}}, C_{\mathrm{SO}}, C_{\mathrm{G}}, C_{\mathrm{W}}) \\ B_{\mathrm{i}} = F_{\mathrm{i}}\left(C_{\mathrm{Sa}} + \frac{h}{2}A_1, C_{\mathrm{Ar}} + \frac{h}{2}A_2, C_{\mathrm{Re}} + \frac{h}{2}A_3, C_{\mathrm{As}} + \frac{h}{2}A_4, C_{\mathrm{SO}} + \frac{h}{2}A_5, C_{\mathrm{G}} + \frac{h}{2}A_6, C_{\mathrm{W}} + \frac{h}{2}A_7\right) \\ C_{\mathrm{i}} = F_{\mathrm{i}}\left(C_{\mathrm{Sa}} + \frac{h}{2}B_1, C_{\mathrm{Ar}} + \frac{h}{2}B_2, C_{\mathrm{Re}} + \frac{h}{2}B_3, C_{\mathrm{As}} + \frac{h}{2}B_4, C_{\mathrm{SO}} + \frac{h}{2}B_5, C_{\mathrm{G}} + \frac{h}{2}B_6, C_{\mathrm{W}} + \frac{h}{2}B_7\right) \\ D_{\mathrm{i}} = F_{\mathrm{i}}(C_{\mathrm{Sa}} + hC_1, C_{\mathrm{Ar}} + hC_2, C_{\mathrm{Re}} + hC_3, C_{\mathrm{As}} + hC_4, C_{\mathrm{SO}} + hC_5, C_{\mathrm{G}} + hC_6, C_{\mathrm{W}} + hC_7) \end{array}\right. \tag{42}$$

Then the following iterative equation can then be used to calculate the MF of the saturated hydrocarbons in section j+1:

$$C_{\mathrm{Sa}}^{j+1} = C_{\mathrm{Sa}}^{j} + \frac{h}{6}(A_1 + 2B_1 + 2C_1 + D_1) \tag{43}$$

where $j = 1,2 \cdots n$.

Similarly, the MF of other lumped substances in the reaction system can be calculated by the above method.

In this paper, the calculation method of the reaction rate constant k is based on the sum of squares of the residual difference between the fitting value and the experimental value. The value of ‘k’ is determined by minimizing this objective function. As shown in Eq. (44) (Dong et al., 2023; Xie et al., 2023a, 2023b).

$$\mathrm{SSR}\left(\overrightarrow{k}\right) = \sum\nolimits_{i=1}^{n}\sum\nolimits_{j=1}^{m}\left(W_{p_i,\ t_j,\ \mathrm{fit}} - W_{p_i,\ t_j,\ \mathrm{experiment}}\right)^2 \tag{44}$$

$$\overrightarrow{k} = \left\{k_1, k_2, k_3, k_4, k_{5\mathrm{f}}, k_{5\mathrm{r}}, k_{6\mathrm{f}}, k_{6\mathrm{r}}, k_{7\mathrm{f}}, k_{7\mathrm{r}}, k_8, k_9, k_{10}, k_{11}\right\} \in (0,1)$$

where $W_{p_i,\ t_j,\ \mathrm{fit}}$ is the MF fitting calculated value of p_i component in t_j time reaction system; $W_{p_i,\ t_j,\ \mathrm{experiment}}$ is the experimental MF of p_i component in t_j time reaction system.

In Python 3.8.7, we formulated a least squares optimization problem for SSR minimization. To minimize the sum of squared residuals and determine the parameters of the kinetic model, we utilized the scipy.optimize.basinhopping function, which combines a global stepping algorithm with local minimization algorithms. During the regression process, the following constraints must be met: all reaction rate constants must adhere to the linear law of the Arrhenius equation. The accuracy of the model is assessed using the coefficient of determination (R^2), as shown in Eq. (45) (Dong et al., 2023; Xie et al., 2023a, 2023b).

$$R^2 = 1 - \frac{\sum_{i=1}^{p} (y_i - \hat{y}_i)^2}{\sum_{i=1}^{p} (y_i - \overline{y}_i)^2} \tag{45}$$

where y_i is the regression to the true value; $\hat{y}$ is the fit the predicted value; $\overline{y}$ is the fit the average of the predicted values.

3.2.2. Fitting and solving of classical segmented reaction dynamics model

The comparison between the experimental results of centimeter sized MLMOS under the action of SCW (380–430 °C) and the fitting values of the classical segmented pyrolysis kinetics model is shown in Fig. 7(a)–(c). The analysis in this paper involves not only comparing the calculated results of the designing time points with the experimental data, but also further calculating the fitted values at 120, 360, and 600 min. The curves shown in Fig. 7(a)–(c) is calculated by smoothly connecting seven operating points. It should be noted that these curves at adjacent operating points do not directly correspond to the calculated values. The determination coefficients obtained at three different temperature conditions are all more than 0.9, which indicates that the traditional segmental pyrolysis reaction kinetic model has high accuracy. Based on this, the reaction rate constant k was calculated and the Arrhenius equation was applied to predict the pre-factor A and activation energy E_a. These calculations are summarized in Table 2. Through the analysis of Tables 2 and it can be found that the reaction rate constants of k_{1f} and k_2 are significantly higher than other reactions, and the value of k_{1f} is lower than k_2. This indicates that the reaction pathway of oil and gas phase formation is the main pathway in organic-rich shales, especially in SCW environment, and the process of gas phase formation is more favorable than oil phase formation. In addition, Table 2 also shows that the value of k_{1r} is greater than k_3, which indicates that the coking reaction path of oil phase substances is more significant than the gasification reaction path. Combining these analysis results, we can conclude that from the classical reaction kinetics simulation results, the gasification trend of organic-rich shale in SCW environment is more obvious, and the contribution of polymerization coking to the reduction of oil content is more significant.

3.2.3. Fitting and solving of refined reaction kinetics model

The comparison between the real pyrolysis experimental results and the fitting settlement results of hydrocarbon generation in the MLMOS of centimeter sized under the action of SCW (380–430 °C) is shown in Fig. 8(a)–(c). The analysis in this paper involves not only comparing the calculated results of the designing time points with the experimental data, but also further calculating the fitted values at 120, 360, and 600 min. The curves shown in Fig. 8(a)–(c) is calculated by smoothly connecting seven operating points. It should be noted that these curves at adjacent operating points do not directly correspond to the calculated values. Under the three different temperature conditions, the obtained coefficient of determination is more than 0.9, which indicates that the new refined model has a high accuracy.

Accordingly, when the reaction rate constant k is solved, through the Arrhenius formula for forecasting refers to the former factor A and activation energy E_a.

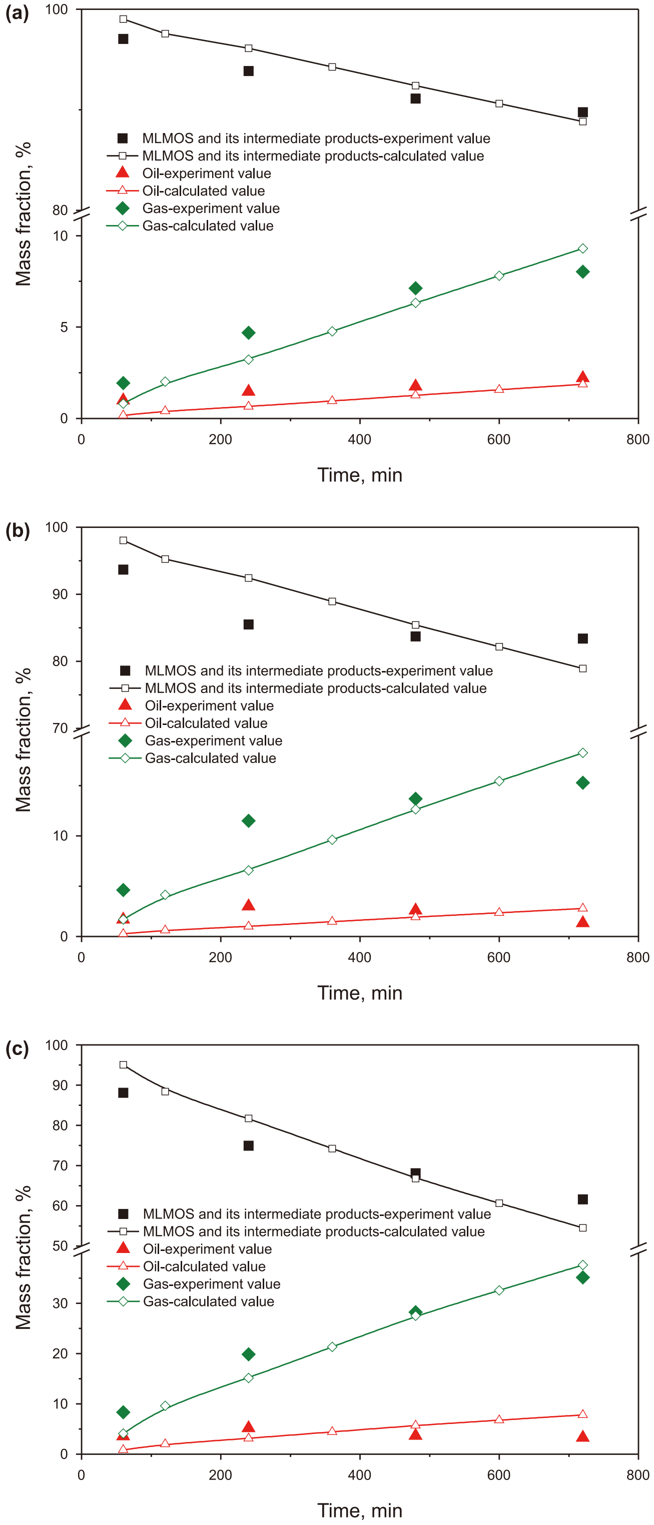

Fig. 7. **(a)** Fitting curves of the classical segmented pyrolysis kinetics model at 380 °C ($R^2 = 0.93$); **(b)** Fitting curves of the classical segmented pyrolysis kinetics model 400 °C ($R^2 = 0.92$); **(c)** Fitting curves of the classical segmented pyrolysis kinetics model 430 °C ($R^2 = 0.92$).

The fitting solution results are shown in Table 3. The main reaction paths of hydrocarbon generation in SCW of massive shale are shown in Fig. 9. The main reaction path of centimeter sized MLMOS

Table 2
Fitting results of classical segmental pyrolysis reaction kinetics model.

k, min^{-1}	Temperature, °C			A	E_a	R^2
	380	400	430			
k_{1f}	2.76×10^{-5}	4.35×10^{-5}	1.45×10^{-4}	1.07×10^{3}	1.29×10^{2}	9.76×10^{-1}
k_{1r}	1.93×10^{-11}	9.80×10^{-11}	3.01×10^{-10}	6.03×10^{5}	2.05×10^{2}	9.58×10^{-1}
k_2	1.37×10^{-4}	2.85×10^{-4}	6.97×10^{-4}	1.07×10^{6}	1.24×10^{2}	9.98×10^{-1}
k_3	6.70×10^{-7}	1.21×10^{-6}	3.10×10^{-6}	1.56×10^{3}	1.17×10^{2}	9.99×10^{-1}

in SCW can be inferred by the reaction rate constant.

As can be seen from Table 3, the results of this study are consistent with the hypothesis of segmented pyrolysis, that is, asphaltene participates in a series of continuous re-pyrolysis processes as an intermediate product of the pyrolysis reaction. k_1 is significantly greater than k_4, which once again verify that the MLMOS can be directly transformed into a large number of stable substances, namely saturated hydrocarbons, in the SCW environment. The reaction path of generating saturated hydrocarbons is still dominant compared with the generation of asphalt intermediates. k_{5f} indicates that another source of saturated hydrocarbons is the pyrolysis of asphalt intermediates. Combined with k_2, k_3, k_{6f} and k_{7f}, it can be concluded that aromatic hydrocarbons and resin mainly come from the pyrolysis of asphalt intermediates. Combined with k_8, k_9, k_{10} and k_{11}, it can be concluded that gas mainly comes from the pyrolysis of saturated hydrocarbons, resin and asphaltene. In addition, it is not difficult to find that k_{5r} and k_{6r} maintain a large value at different temperatures, which indicates that during the hydrocarbon generation process, the main sources of asphaltenes are in addition to kerogen pyrolysis and resin polymerization, the polymerization of saturated hydrocarbon and aromatic hydrocarbon is also the main source of asphaltenes.

Through the above analysis can be found that the hydrocarbon generation process of centimeter sized MLMOS in the SCW environment mainly includes the direct conversion of these shales into asphaltene and saturated hydrocarbons; Asphaltene is further pyrolyzed to produce saturated hydrocarbons, aromatics and resins. Asphaltene is formed by polymerization of saturated hydrocarbon, aromatic hydrocarbon and resin. And the interaction of saturated hydrocarbons, resins and asphaltenes to produce gases.

On the whole, compared with previous research results on hydrocarbon generation kinetics of millimeter sized MLMOS in SCW atmosphere (Xie et al., 2023a, 2023b), the hydrocarbon generation reaction path of centimeter sized MLMOS in SCW is basically similar to that of millimeter sized MLMOS in SCW. The hydrocarbon generation pathways of millimeter medium and low maturity organic-rich shale in supercritical water mainly consisted of direct generation of asphaltenes and saturated hydrocarbons from kerogen, pyrolysis of asphaltenes to saturated hydrocarbons, aromatic hydrocarbons, and resins, polymerization of resins to asphaltenes, and gas generation from saturated hydrocarbons, resins, and asphaltenes (Xie et al., 2023a, 2023b). However, the difference between the hydrocarbon generation path of millimeter sized MLMOS and centimeter sized MLMOS is that the asphaltene formation path is different. The reaction path of asphaltene formation in millimeter sized MLMOS in the presence of supercritical water is mainly the pyrolysis of kerogen and the polymerization of resin. The reaction path of asphaltene formation in centimeter sized MLMOS in the presence of supercritical water is mainly pyrolysis of MLMOS, polymerization of saturated hydrocarbon, aromatic hydrocarbon and resin.

The reasons for this difference may be as follows: It has been proved that in the pyrolysis process of oil shale, the reaction of pyrolysis of macromolecular organic matter into small molecular matter coexists with the reaction of polymerization of small molecular matter into large molecular matter (Liang et al., 2021). Shale is a dense rock with extremely low internal permeability. When macromolecular organic matter is in-situ pyrolyzed, it needs to be released into the outer space of shale through pore channels to enter the supercritical water environment. The increase in shale size leads to an increase in release distance and release time. In other words, before the small molecule organic matter generated by in-situ pyrolysis is released into the outer space of shale, it has to go through a reaction environment where no water exists, which promotes the advantage of polymerization reaction, which has also been confirmed by previous studies (Xie et al., 2022, 2023a, 2023b). When the organic matter enters the supercritical water atmosphere, the polymerization reaction is effectively inhibited. Therefore, for millimeter sized shale, saturated hydrocarbon and aromatic hydrocarbon are quickly released into supercritical water environment after in-situ formation in shale pores, and further pyrolysis into smaller molecules of gas. In this case, the pyrolysis reaction of saturated hydrocarbon and aromatic hydrocarbon occupies a significant dominant position. For centimeter sized shale, saturated hydrocarbon and aromatic hydrocarbon stay longer in the pore channel after in-situ formation, and the polymerization reaction could not be ignored, which leads to the main source path of asphaltene.

3.3. Model accuracy evaluation

3.3.1. Classical segmented pyrolysis reaction kinetic model

For the classical hydrocarbon generation kinetics model of centimeter-level MLMOS in SCW environment, the error or accuracy of the model can be analyzed by making the following graph. the data on the horizontal axis represent values obtained in real experiments, and the data on the vertical axis represent the calculated value according to specific working conditions, as shown in Fig. 10. It can be observed from Fig. 10 that the values obtained by the experiment are very close to those obtained by the fitting calculation, and the determination coefficients obtained by fitting experimental data at 380, 400 and 430 °C are 0.93, 0.92 and 0.92, respectively, indicating that the traditional staged pyrolysis kinetic model still has high accuracy under the condition of SCW.

Similarly, in order to further confirm the accuracy of the traditional reaction kinetics model in the SCW environment, the prediction of this model can be compared with the experimental data. This is the most direct means of verification. A set of predicted data can be obtained by comparing the data predicted by the model for the change of the mass score over time under different conditions. Taking the working condition of 390 °C as an example, these predicted data are compared with the actual experimental data. As shown in Figs. 11 and 12, the prediction curve is in good agreement with the experimental data. However, the error analysis reveals that the prediction error of the traditional kinetic model is large at the initial stage of the reaction, but the error decreases gradually with the increase of the reaction time. This error may be related to the complex material composition and structure of organic-rich

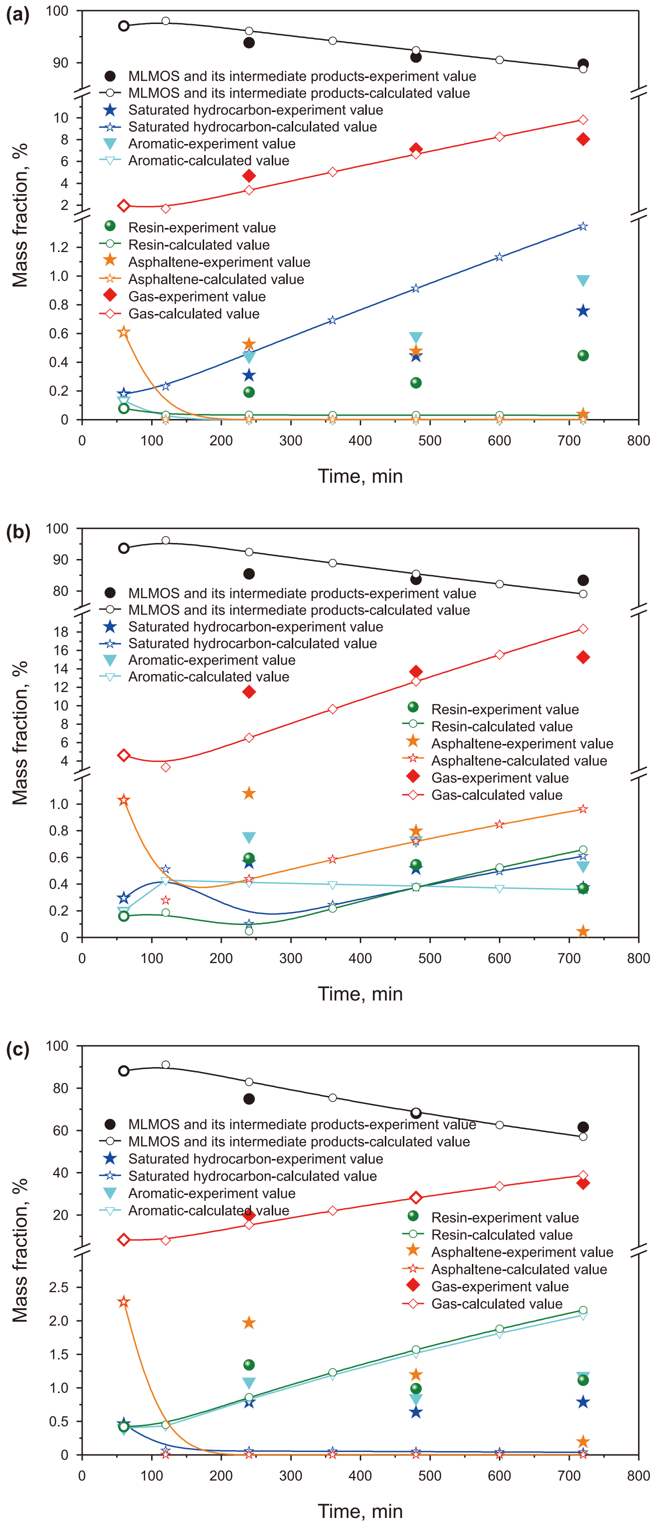

Fig. 8. **(a)** Fitting curves of the new refined pyrolysis kinetics model at 380 °C ($R^2 = 0.90$); **(b)** Fitting curves of the new refined pyrolysis kinetics model at 400 °C ($R^2 = 0.91$); **(c)** Fitting curves of the new refined pyrolysis kinetics model at 430 °C ($R^2 = 0.91$).

shale. When the reaction time reaches 12 h, the relative errors between the experimental and predicted values of oil and gas phase products are less than 25%, which indicates that the traditional segmental pyrolysis kinetic model can accurately predict the distribution of hydrocarbon products under long-term reaction conditions.

3.3.2. *Refined reaction kinetics model*

Similar to the hydrocarbon generation kinetics model used to evaluate MLMOS of millimeters in SCW, the fine hydrocarbon generation kinetics model of MLMOS of centimeters in SCW has the horizontal axis representing experimental data and the vertical axis representing calculated values, as shown in Fig. 13. Ideally, when all the points are clustered around the line Y = X, it indicates that the model has good prediction accuracy. However, due to the complexity of actual influencing factors, it is difficult to develop a completely accurate hydrocarbon dynamics model.

It can be seen from Fig. 13 that all points are closely distributed around Y = X line. Through the fitting process, we calculate the determination coefficients at 380, 400 and 430 °C, which are 0.90, 0.91 and 0.91 respectively. These results confirm the accuracy of the refined reaction kinetics model established in this paper for MLMOS under SCW conditions.

Similarly, in order to verify the accuracy of the fine reaction kinetics model constructed in this paper from more perspectives, we first calculated the data of working conditions other than the working conditions used in this paper, and then carried out experiments under the conditions of the working conditions, and compared the experimental data with the fitting data. We obtain a set of fitting calculation data for the change of MF with reaction time at a temperature of 390 °C. The results are shown in Figs. 14 and 15. The results show that the predicted curves are in good agreement with the experimental data, although the relative errors show large deviations in the MF of saturated hydrocarbons, aromatics, resins and asphaltenes. This indicates that the accuracy of the model in predicting the distribution of oil components in shale under the action of SCW needs to be further optimized. However, if the distribution of oil and gas phase products is analyzed from a macroscopic perspective, it can be found that the relative error between the experimental value and the model prediction value is usually less than 14%. This shows that the model can accurately predict the distribution of oil and gas products produced by shale with low maturity and rich organic matter under SCW conditions. Compared with the prediction error of millimeter sized shale, the distribution model of oil and gas phase products of centimeter shale shows a slightly higher prediction error. This difference highlights the more complex effects of increasing shale size on hydrocarbon generation processes and the need for more in-depth studies to improve the prediction accuracy of models.

4. Conclusion

In this paper, the effects of temperature and reaction time on hydrocarbon generation in the process of co-heating of SCW and MLMOS were investigated by using a set of self-developed heating reaction device. According to the data obtained from the above experiments, the classical segmented pyrolysis reaction kinetics model and the new refined reaction kinetics model were established and solved by fitting. The conclusions are as follows.

(1) Under the condition of SCW in-situ conversion, the classical segmented pyrolysis kinetics model had low prediction accuracy for hydrocarbon product distribution at the initial stage of the reaction. The prediction accuracy increased

Table 3
The solution results of the kinetics parameters of the refined reaction kinetics model are obtained.

k, min^{-1}	Temperature, °C			A	E_a	R^2
	380	400	430			
k_1	4.70×10^{-5}	1.00×10^{-4}	1.81×10^{-4}	1.01×10^{2}	6.59×10^{3}	9.74×10^{-1}
k_2	1.00×10^{-16}	1.00×10^{-16}	1.00×10^{-16}	-	-	-
k_3	3.18×10^{-15}	7.39×10^{-15}	2.03×10^{-14}	1.69×10^{3}	1.41×10^{2}	9.98×10^{-1}
k_4	1.64×10^{-7}	7.39×10^{-7}	1.75×10^{-6}	2.65×10^{7}	1.77×10^{2}	9.39×10^{-1}
k_{5f}	9.64×10^{-5}	1.35×10^{-3}	7.11×10^{-3}	6.65×10^{21}	3.21×10^{2}	9.50×10^{-1}
k_{5r}	8.52×10^{-9}	4.85×10^{-7}	3.58×10^{-6}	1.15×10^{28}	4.48×10^{2}	9.20×10^{-1}
k_{6f}	1.35×10^{-7}	3.36×10^{-6}	4.29×10^{-5}	7.70×10^{27}	4.33×10^{2}	9.74×10^{-1}
k_{6r}	5.23×10^{-8}	4.85×10^{-7}	1.30×10^{-6}	7.63×10^{11}	2.38×10^{2}	9.04×10^{-1}
k_{7f}	2.96×10^{-6}	4.56×10^{-5}	4.67×10^{-4}	1.16×10^{25}	3.81×10^{2}	9.80×10^{-1}
k_{7r}	6.81×10^{-4}	6.08×10^{-3}	2.11×10^{-2}	2.66×10^{17}	2.56×10^{2}	9.38×10^{-1}
k_8	1.93×10^{-11}	1.35×10^{-9}	8.77×10^{-9}	6.48×10^{25}	4.53×10^{2}	9.04×10^{-1}
k_9	2.01×10^{-16}	2.72×10^{-15}	1.18×10^{-14}	5.26×10^{8}	3.03×10^{2}	9.37×10^{-1}
k_{10}	1.17×10^{-3}	6.63×10^{-3}	2.20×10^{-2}	5.40×10^{14}	2.20×10^{2}	9.61×10^{-1}
k_{11}	1.28×10^{-2}	2.87×10^{-2}	6.99×10^{-2}	2.68×10^{8}	1.29×10^{2}	9.96×10^{-1}

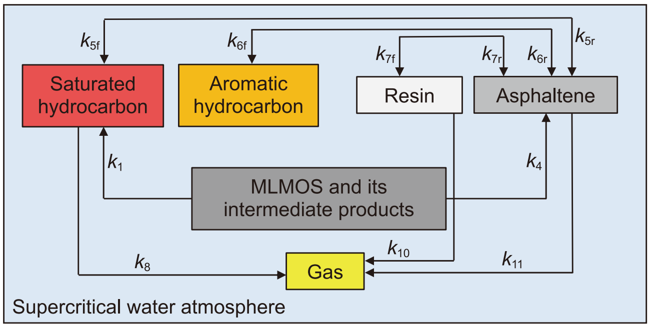

Fig. 9. Hydrocarbon generation reaction network between MLMOS and SCW.

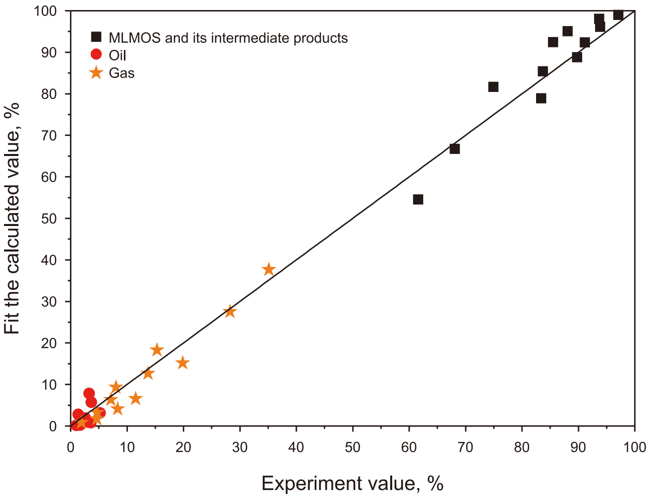

Fig. 10. Error analysis between fitted values and experimental values.

gradually with increasing reaction time. When the reaction time was 12 h, the error can reach less than 25%.

(2) The new refined reaction kinetics model can accurately predict the distribution of oil and gas products in organic-rich shale under SCW in-situ conversion, and the prediction error can be less than 14%.

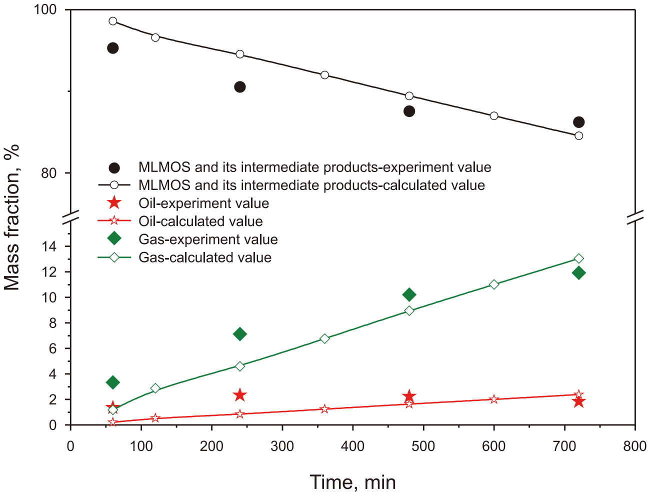

Fig. 11. Prediction of product distribution at 390 °C.

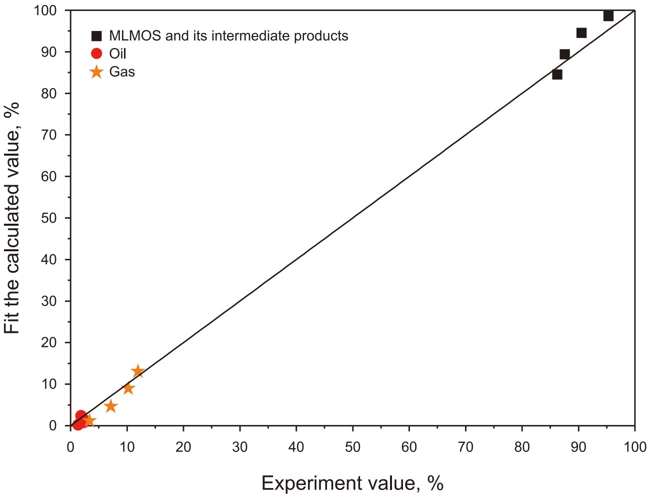

Fig. 12. Prediction accuracy analysis of product distribution at 390 °C.

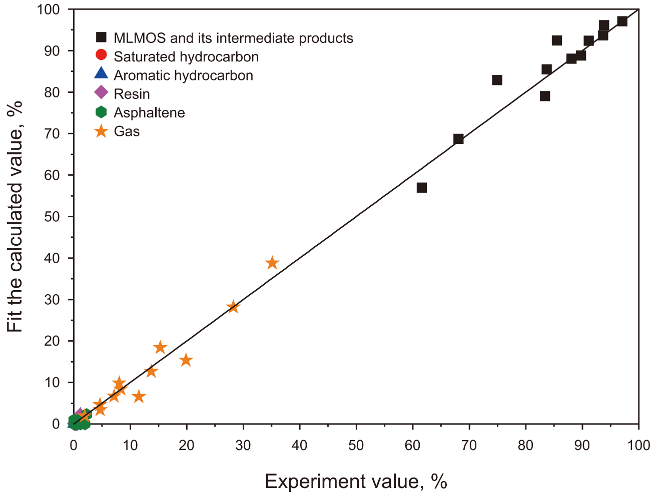

Fig. 13. Analysis of fitting accuracy under three temperature conditions.

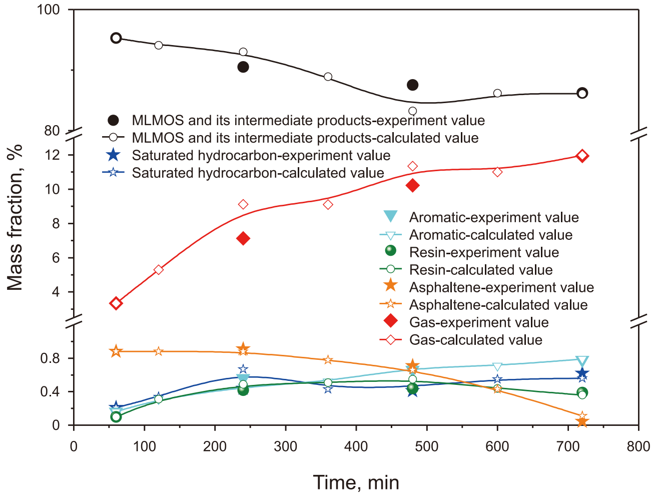

Fig. 14. Prediction of product distribution at 390 °C.

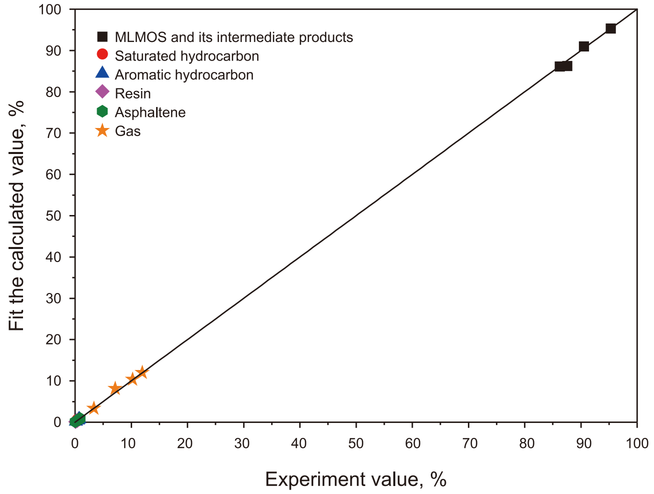

Fig. 15. Prediction accuracy analysis of product distribution at 390 °C.

(3) The reaction paths of centimeter sized MLMOS in SCW mainly include: MLMOS directly generated asphaltene and saturated hydrocarbon. Asphaltene pyrolysis generated saturated hydrocarbon, aromatic hydrocarbon and resin. Saturated hydrocarbon, aromatic hydrocarbon and resin polymerization generated asphaltene, and saturated hydrocarbon, resin and asphaltene generated gas.

CRediT authorship contribution statement

Tian Xie: Writing – review & editing, Writing – original draft, Methodology, Investigation. **Qiu-Yang Zhao:** Methodology, Investigation. **Hui Jin:** Methodology. **Ye-Chun Wang:** Investigation. **Lie-Jin Guo:** Methodology, Funding acquisition.

Declaration of competing interest

The authors declare that they have no known competing financial interests or personal relationships that could have appeared to influence the work reported in this paper.

Acknowledgments

The financial support by the Basic Science Center Program of the Ordered Energy Conversion of the National Nature Science Foundation of China (NO. 52488201) is gratefully acknowledged.

References

Akiya, N., Savage, P.E., 2002. Roles of water for chemical reactions in high-temperature water. Chem. Rev. 102, 2725–2750. https://doi.org/10.1021/cr000668w.

Bar, H., Ikan, R., Aizenshtat, Z., 1988. Comparative study of the isothermal pyrolysis kinetic behaviour of some oil shales and coals. J. Anal. Appl. Pyrolysis. 14, 49–71. https://doi.org/10.1016/0165-2370(88)80007-X.

Brandt, A.R., 2008. Converting oil shale to liquid fuels: energy inputs and greenhouse gas emissions of the Shell in situ conversion process. Environ. Sci. Technol. 42, 7489. https://doi.org/10.1021/es800531f.

Chen, W., Hu, T.Q., Xu, G.Y., Gu, L.B., Xiao, F.Y., Fang, B.Z., Zhong, X.H., Chen, B.L., 2024. Co-combustion of furfural residue waste and oil shale: characteristics, synergistic effects, kinetics, and optimization analysis. Biomass Conversion and Biorefinery 14 (13), 14447–14461. https://doi.org/10.1007/s13399-023-04037-8.

Dong, Y., Zhao, Q.Y., Zhou, Y.T., Zheng, L.C., Jin, H., Baercheng, B., Guo, L.J., 2023. Kinetic study of asphaltenes phase separation in supercritical water upgrading of heavy oil. Fuel Process. Technol. 241, 107588. https://doi.org/10.1016/j.fuproc.2022.107588.

Deng, S., Wang, Z., Gao, Y., et al., 2012. Subcritical water extraction of bitumen from Huadian oil shale lumps. J. Anal. Appl. Pyrolysis 98, 151–158. https://doi.org/10.1016/j.jaap.2012.07.011.

Fang, C., Li, S., Ma, G., et al., 2012. Reaction mechanism and kinetics of pressurized pyrolysis of Chinese oil shale in the presence of water. Pet. Sci. 9, 532–534. https://doi.org/10.1007/s12182-012-0239-0.

Flynn, J.H., Wall, L.A., 1966. General treatment of the thermogravimetry of polymers. J. Res. Natl. Bur. Stand., Sect. A 70A, 487–523. https://doi.org/10.6028/jres.070A.043.

Guo, L., Jin, H., Lu, Y., 2015. Supercritical water gasification research and development in China. J. Supercrit. Fluids 96, 144–150. https://doi.org/10.1016/j.supflu.2014.09.023.

Guo, W., Zhu, B., Liu, Z., et al., 2024. Fracture propagation and evaluation of dual wells, multi-fracturing, and split-time in Fuyu oil shale. Geoenergy Science and Engineering 239, 212948. https://doi.org/10.1016/j.geoen.2024.212948.

Hou, L., Ma, W., Luo, X., et al., 2020. Characteristics and quantitative models for hydrocarbon generation-retention-production of shale under ICP conditions: example from the Chang 7 member in the Ordos Basin. Fuel 279, 118497. https://doi.org/10.1016/j.fuel.2020.118497.

Huang, D., Kang, Z., Yang, Z., 2023. Study on the pyrolysis behavior and kinetics of Jimusar oil shale with H_2O/CO_2 injection. Oil Shale 40 (4), 321–343. https://doi.org/10.3176/oil.2023.4.03.

Hu, H., Zhang, J., Guo, S., et al., 1999. Extraction of Huadian oil shale with water in sub- and supercritical states. Fuel 78, 645–651. https://doi.org/10.1016/S0016-2361(98)00199-9.

Hu, X., Lu, Y., Li, W., et al., 2024. Study on the pyrolysis behavior and product characteristics of Balikun oil shale with different water pressures in sub- and supercritical states. Fuel 369, 131701. https://doi.org/10.1016/j.fuel.2024.131701.

Jin, Z., Bai, Z., Gao, B., et al., 2019. Has China ushered in the shale oil and gas revolution? Oil Gas Geol. 40, 451–458. https://doi.org/10.11743/ogg20190301.

Kang, X., Ye, G., Zhu, S., 2024. Optimization and kinetic analysis of direct alkali leaching of silica from vanadium-bearing shale leaching residue. Silicon 16 (8), 3217–3231. https://doi.org/10.1007/s12633-024-02916-x.

Kang, Z., Zhao, Y., Yang, D., 2020a. Review of oil shale in-situ conversion technology. Appl. Energy 269, 115121. https://doi.org/10.1016/j.apenergy.2020.115121.

Kang, Z., Zhao, Y., Yang, D., et al., 2020b. A pilot investigation of pyrolysis from oil and gas extraction from oil shale by in-situ superheated steam injection. J. Pet. Sci. Eng. 186, 106785. https://doi.org/10.1016/j.petrol.2019.106785.

Li, S., Yue, C., 2003. Study of pyrolysis kinetics of oil shale. Fuel 82, 337–342. https://doi.org/10.1016/S0016-2361(02)00268-5.

Liang, X., Zhao, Q., Dong, Y., et al., 2021. Experimental investigation on supercritical water gasification of organic-rich shale with low maturity for syngas production. Energy & Fuels 35, 7657–7665. https://doi.org/10.1021/acs.energyfuels.0c04140.

Lin, Y., Liao, Y., Yu, Z., 2016. Co-pyrolysis kinetics of sewage sludge and oil shale thermal decomposition using TGA-FTIR analysis. Energy Convers. Manage. 118, 345–352. https://doi.org/10.1016/j.enconman.2016.04.004.

Ma, Y., Li, S., 2018. The mechanism and kinetics of oil shale pyrolysis in the presence of water. Carbon Resour Convers. 1 (2), 160–164. https://doi.org/10.1016/j.crcon.2018.04.003.

Nasyrova, Z.R., Kayukova, G.P., Onishchenko, Y.V., et al., 2020. Conversion of high-carbon domanic shale in sub- and supercritical waters. Energy & Fuels 34, 1329–1336. https://doi.org/10.1021/acs.energyfuels.9b03130.

Ozawa, T., 1965. A new method of analyzing thermogravimetric data. Bull. Chem. Soc. Jpn. 38, 1881–1886. https://doi.org/10.1246/BCSJ.38.1881.

Rana, R., Nanda, S., Maclennan, A., et al., 2019. Comparative evaluation for catalytic gasification of petroleum coke and asphaltene in subcritical and supercritical water. J. Energy Chem. 31, 107–118. https://doi.org/10.1016/j.jechem.2018.05.012.

Rodriguez, C.C., Kruse, A., 2018. Supercritical water gasification of biomass for hydrogen production- Review. J. Supercrit. Fluids 133, 573–590. https://doi.org/10.1016/j.supflu.2017.09.019.

Reddy, S.N., Nanda, S., Dalai, A.K., et al., 2014. Supercritical water gasification of biomass for hydrogen production. Int. J. Hydrogen Energy 39, 6912–6926. https://doi.org/10.1016/j.ijhydene.2014.02.125.

Sun, Y., Bai, F., Lu, X., et al., 2015. Kinetic study of Huadian oil shale combustion using a multi-stage parallel reaction model. Energy 82, 705–713. https://doi.org/10.1016/j.energy.2015.01.080.

Sun, Y., Kang, S., Wang, S., et al., 2019. Subcritical water extraction of huadian oil shale at 300 °C. Energy & Fuels 33, 2106–2114. https://doi.org/10.1021/acs.energyfuels.8b04431.

Tang, X., Li, S., Yue, C., et al., 2013. Lumping kinetics of hydrodesulfurization and hydrodenitrogenation of the middle distillate from Chinese shale oil. Oil Shale 30, 517–535. https://doi.org/10.3176/OIL.2013.4.05.

Veski, R., Palu, V., Kruusement, K., 2006. Co-liquefaction of kukersite oil shale and pine wood in supercritical water. Oil Shale 23, 236–248. https://doi.org/10.3176/oil.2006.3.04.

Wang, Z., Deng, S., Gu, Q., et al., 2014. Subcritical water extraction of huadian oil shale under isothermal condition and pyrolysate analysis. Energy & Fuels 28, 2305–2313. https://doi.org/10.1021/ef5000062.

Wang, C., Zhu, C., Huang, J., et al., 2021. Enhancement of depolymerization slag gasification in supercritical water and its gasification performance in fluidized bed reactor. Renew. Energy 168, 829–837. https://doi.org/10.1016/j.renene.2020.12.104.

Weingärtner, H., Franck, E.U., 2005. Supercritical water as a solvent. Angew. Chem., Int. Ed. 44, 2672–2692. https://doi.org/10.1002/anie.200462468.

Xie, T., Zhao, Q., Dong, Y., et al., 2022. Experimental investigation on the hydrocarbon generation of low maturity organic-rich shale in supercritical water. Oil Shale 39 (3), 169–188. https://doi.org/10.3176/oil.2022.2.02.

Xie, T., Zhao, Q., Jin, H., et al., 2023a. Reaction kinetics study on hydrocarbon generation of medium-and low-maturity organic-rich shale in supercritical wate. Energy & Fuels 37, 14192–14201. https://doi.org/10.1021/acs.energyfuels.3c02494.

Xie, T., Zhao, Q., Dong, Y., et al., 2023b. Experimental investigation on hydrocarbon generation of organic-rich shale with low maturity in sub- and supercritical water. Geoenergy Science and Engineering 223, 211553. https://doi.org/10.1016/j.geoen.2023.211553.

Yanik, J., Yuksel, M., Saglam, M., et al., 1995. Characterization of the oil fractions of shale oil obtained by pyrolysis and supercritical water extraction. Fuel 74, 46–50. https://doi.org/10.1016/0016-2361(94)P4329-Z.

Zou, C., Yang, Z., Cui, J., et al., 2013. Formation mechanism, geological characteristics and development strategy of nonmarine shale oil in China. Pet. Explor. Dev. 40, 15–27. https://doi.org/10.1016/S1876-3804(13)60002-6.

Zhao, Q., Guo, L., Huang, Z., et al., 2018. Experimental investigation on enhanced oil recovery of extra heavy oil by supercritical water flooding. Energy & Fuels 32, 1685–1692. https://doi.org/10.1021/acs.energyfuels.7b03839.

Zhao, S., Pu, W., Varfolomeev, M.A., 2022. Influence of water on thermo-oxidative behavior and kinetic triplets of shale oil during combustion. Fuel 318, 123690. https://doi.org/10.1016/j.fuel.2022.123690.

Zhao, W., Hu, S., Hou, L., et al., 2020. Types and resource potential of continental shale oil in China and its boundary with tight oil. Pet. Explor. Dev. 47, 1–11. https://doi.org/10.11698/PED.2020.01.01.

Zheng, Y., Lei, G., Yao, C., et al., 2023. Characteristics and kinetics of Maoming oil shale pyrolysis in the presence of $CoCl_2$ assisted steam. Fuel 338, 127279. https://doi.org/10.1016/j.fuel.2022.127279.